Scaling for Saturated Moist Quasigeostrophic Turbulence

MARGUERITE L. BROWN,[a] OLIVIER PAULUIS,[a] AND EDWIN P. GERBER[a]

[a] *Center for Atmosphere Ocean Science, Courant Institute of Mathematical Sciences, New York University, New York, New York*

(Manuscript received 30 September 2022, in final form 1 March 2023, accepted 7 March 2023)

ABSTRACT: Much of our conceptual understanding of midlatitude atmospheric motion comes from two-layer quasigeostrophic (QG) models. Traditionally, these QG models do not include moisture, which accounts for an estimated 30%–60% of the available energy of the atmosphere. The atmospheric moisture content is expected to increase under global warming, and therefore, a theory for how moisture modifies atmospheric dynamics is crucial. We use a two-layer moist QG model with convective adjustment as a basis for analyzing how latent heat release and large-scale moisture gradients impact the scalings of a midlatitude system at the synoptic scale. In this model, the degree of saturation can be tuned independently of other moist parameters by enforcing a high rate of evaporation from the surface. This allows for study of the effects of latent heat release at saturation, without the intrinsic nonlinearity of precipitation. At saturation, this system is equivalent to the dry QG model under a rescaling of both length and time. This predicts that the most unstable mode shifts to smaller scales, the growth rates increase, and the inverse cascade extends to larger scales. We verify these results numerically and use them to verify a framework for the complete energetics of a moist system. We examine the spectral features of the energy transfer terms. This analysis shows that precipitation generates energy at small scales, while dry dynamics drive a significant broadening to larger scales. Cascades of energy are still observed in all terms, albeit without a clearly defined inertial range.

SIGNIFICANCE STATEMENT: The effect of moist processes, especially the impact of latent heating associated with condensation, on the size and strength of midlatitude storms is not well understood. Such insight is particularly needed in the context of global warming, as we expect moisture to play a more important role in a warmer world. In this study, we provide intuition into how including condensation can result in midlatitude storms that grow faster and have features on both larger and smaller scales than their dry counterparts. We provide a framework for quantifying these changes and verify it for the special case where it is raining everywhere. These findings can be extended to the more realistic situation where it is only raining locally.

KEYWORDS: Atmosphere; Turbulence; Precipitation; Moisture/moisture budget

1. Introduction

A major challenge to our understanding of midlatitude storm systems lies in the interplay between the atmospheric circulation and the hydrological cycle. On a global scale, higher temperature and humidity in the tropics relative to the poles drives poleward transport of both sensible and latent heat. On the local scale, ascending parcels undergo adiabatic expansion, condensing excess moisture to release latent heat. This additional energy can induce local hydrodynamical instabilities in conditions that would otherwise be stable. The effect of moisture is not isolated to the scales on which condensation occurs, but rather impacts dynamics across a broad range of scales, including the aggregate behavior of storm tracks (Shaw et al. 2016), the extratropical stratification (Frierson et al. 2006; Schneider and O'Gorman 2008; Wu and Pauluis 2014), and the global atmospheric circulation (Pauluis et al. 2010). Understanding the impacts of moist processes across the full range of geophysical scales is necessary to understand how midlatitude storm dynamics will change in a world becoming more humid as a result of climate change.

Many previous studies have focused on scale changes associated with moisture. Stronger moist effects lead to smaller-scale motions and narrower regions of saturation (Emanuel et al. 1987; Fantini 1990; Lapeyre and Held 2004). This correlation obfuscates the effect of different mechanisms by which moisture induces smaller-scale motion. For instance, does the shift arise as a result of highly localized precipitation associated with the cascade of moisture to small scales? Would a similar result persist even if the precipitation characteristically occurred on larger scales? And how do nonlinearities in precipitation and Clausius–Clapeyron change the dynamics? Many studies also reach opposite conclusions regarding the impact of moisture. For instance, moisture's impact on eddy kinetic energy has been found to be positive (Emanuel et al. 1987; Lapeyre and Held 2004; Lambaerts et al. 2011), negative (Zurita-Gotor 2005; Bembenek et al. 2020; Lutsko and Hell 2021), or about neutral (Lambaerts et al. 2012).

Questions remain about how to synthesize results from different implementations of moisture in idealized systems. The construction and interpretation of a moist energy (ME) and moist potential vorticity (MPV) are key pieces that can help bridge this gap. The changes moisture introduces to the energetics result in changes to the scale at which energy is injected into the flow, its ability to cascade to different scales, and the scale at which it is dissipated. Furthermore, because moisture introduces new processes, moist systems feature new mechanisms of growth and propagation, the impact of which must

Corresponding author: Marguerite Brown, mlb542@nyu.edu

DOI: 10.1175/JAS-D-22-0215.1

be understood both individually and in combination. To this end, the study of moist turbulence benefits from a hierarchy of models with implementations of moisture mechanisms in different combinations and at different levels of complexity, including both linear (Emanuel et al. 1987; Adames and Ming 2018; Adames 2021) and nonlinear (Fantini 1990; Lapeyre and Held 2004) frameworks.

The two-layer quasigeostrophic (QG) model is one of the simplest mathematical models to exhibit the basic features of the turbulent midlatitude atmosphere, from planetary-scale barotropic jets to synoptic-scale baroclinic eddies that organize into storm tracks. Its relative simplicity, coupled with its ability to capture key dynamical features, has made it a good choice for studying the broader statistical and scaling properties of a dry atmosphere (e.g., Vallis 2006). While its utility in assessing the moist case is limited due to significant ageostrophy in precipitation regions (Fantini 1990, 1995; Lambaerts et al. 2011, 2012), moist QG (MQG) models can still provide insight into the dynamics without confounding influences from the tropics. Consequently, MQG models have been used in studies of the fundamental dynamics of baroclinic systems, such as mechanisms of growth (Parker and Thorpe 1995; Moore and Montgomery 2004; de Vries et al. 2010; Adames and Ming 2018) and analysis of turbulent spectra (Edwards et al. 2019). MQG systems are also ideal for developing theories of wave–mean flow interaction in moist systems, which is the portion of theory we seek to advance in this paper.

We use the MQG model of Lapeyre and Held (2004) to bring new intuition to the impacts of moisture on geostrophic turbulence. In section 2, we review the model and derive a conservation law for a moist potential vorticity. We argue that in the limit of high evaporation rate, the model approaches a saturated limit with precipitation active everywhere. We show in appendix A that this saturated limit is mathematically equivalent to the classic two-layer problem after replacing the baroclinic potential vorticity by the MPV, and rescaling both the horizontal and temporal dimensions. In particular, existing theory for dry QG turbulence can be readily tested in the MQG model in the saturated limit.

In section 3, we discuss the numerical implementation of the MQG model and analyze the results of numerical simulations. We show that increasing the amount of moisture leads to three main effects: a systematic intensification of turbulence, a shift of energy injection to smaller scales, and an extension of the inverse cascade to larger scales. In section 4, we analyze the energetics of the MQG model and derive an expression for ME that is converted into available potential energy (APE) through precipitation. We show that the intensification of turbulence with increased moisture is directly tied to the increased generation of ME by the barotropic flow acting on the mean temperature and humidity gradient. In section 5, we argue that the shift of the most unstable baroclinic mode in the linear instability analysis is reflected by the shift in the precipitation injection scale. We derive an expression for the Rhines scale in the saturated limit by accounting for the additional generation of ME and show that this captures the impact of moisture on the energy containing scale in our simulations. The study concludes in section 6.

2. Model description

We use the two-layer MQG model of Lapeyre and Held (2004), depicted schematically in Fig. 1. This model consists of two well-stratified layers of equal mean depth H in a doubly periodic domain. Rotational dynamics are captured by a β plane in which the Coriolis parameter is expressed linearly in the meridional coordinate as $f = f_0 + \beta y$. For guidance, a list of key variables and their definitions can be found in Table 1.

a. The dry system

The classic two-layer QG system has been explored in depth (e.g., Vallis 2006). The flow of such a system can be decomposed into a barotropic streamfunction $\psi_{\mathrm{BT}} = (\psi_1 + \psi_2)/2$, the column-integrated "bulk" movement, and a baroclinic streamfunction $\psi_{\mathrm{bc}} = (\psi_1 - \psi_2)/2$, the vertical gradient. The corresponding geostrophic velocities are given by $(u_i, v_i) = (-\partial_y \psi_i, \partial_x \psi_i)$ in mode i = BT, bc, and the corresponding vorticities $\zeta_i = \nabla^2 \psi_i$. The vorticities evolve as

$$\frac{D_{\mathrm{BT}}}{Dt}(\zeta_{\mathrm{BT}} + \beta y) = -J(\psi_{\mathrm{bc}}, \zeta_{\mathrm{bc}}) - \frac{r}{2}(\zeta_{\mathrm{BT}} - \zeta_{\mathrm{bc}}), \tag{1}$$

$$\frac{D_{\mathrm{BT}}}{Dt}\zeta_{\mathrm{bc}} = -J(\psi_{\mathrm{bc}}, \zeta_{\mathrm{BT}} + \beta y) - f_0 \frac{W}{H} + \frac{r}{2}(\zeta_{\mathrm{BT}} - \zeta_{\mathrm{bc}}). \tag{2}$$

Here, $J(\cdot\,,\,\cdot)$ indicates the Jacobian and $D_{\mathrm{BT}}/Dt = \partial t + J(\psi_{\mathrm{BT}}, \cdot)$ indicates the material derivative with respect to the barotropic flow. Both the barotropic and baroclinic vorticities are advected by the barotropic flow and forced by nonlinear interactions between the two modes characterized by the first term of the right-hand side. Baroclinic vorticity is additionally generated when the ageostrophic convergence W/H, explicitly defined in appendix B, transports mass between the two layers. Mass is transported upward (downward) when W is positive (negative), corresponding with a generation of anticyclonic (cyclonic) baroclinic vorticity. Finally, Ekman damping at the bottom

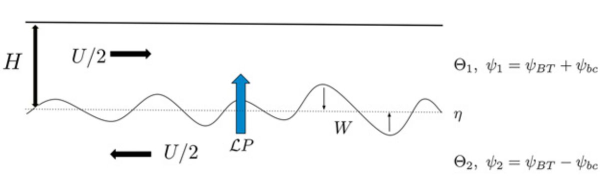

FIG. 1. Structure of the two-layer model. Thick flat lines correspond to surfaces that remain fixed and the wavy curve to the interface η, which varies. Each layer has a streamfunction relating to the barotropic and baroclinic modes as described in the text, an associated potential temperature, and a typical height scale H. The interface η captures variations from this typical thickness, which are corrected by vertical motion W. The moisture m is confined to the lower layer and precipitation conditionally triggers mass transport $\mathcal{L}P$ from the bottom to the top layer. Ekman dissipation $r\nabla^2(\psi_{\mathrm{BT}} - \psi_{\mathrm{bc}})$ takes effect at the bottom surface.

TABLE 1. Variables used in the model description.

Variable	Meaning
ψ_i	Streamfunction of the ith mode, i = BT, bc for barotropic and baroclinic
ζ_i	Vorticity of the ith mode, i = BT, bc for barotropic and baroclinic
W	Low-level convergence; a proxy for vertical motion
H	Interface between the top and bottom layers; a proxy for temperature
q_i	Potential vorticity (PV) of the ith mode, i = BT, bc, m for barotropic, baroclinic, and moist baroclinic
m	Thickness equivalent moist mixing ratio
η_c	Condensation level
m_s	Saturation mixing ratio
P	Precipitation
E	Evaporation

surface predominantly dissipates barotropic vorticity at large scales.

The interface η between the two layers acts as a proxy for temperature, evolving with both the vertical and horizontal transport of mass. Thermal wind balance relates this interface to the baroclinic mode

$$\eta = \frac{2H}{\lambda^2 f_0}\psi_{bc}, \tag{3}$$

where $\lambda = \sqrt{g^* H}/f_0$ is the Rossby deformation radius and $g^* = g\delta\theta/\theta_0$ the reduced gravity. The interface evolves as

$$\frac{D_{\mathrm{BT}}}{Dt}\eta = -W + S, \tag{4}$$

where S indicates the total diabatic forcing, including both radiative cooling and latent heat release.

Equations (2) and (4) can be combined to eliminate the ageostrophic divergence term. This leads to the potential vorticity (PV), defined for the barotropic mode as $q_{\mathrm{BT}} = \zeta_{\mathrm{BT}} + \beta y$; and for the baroclinic mode as $q_{\mathrm{bc}} = \zeta_{\mathrm{bc}} - f_0\eta/H$. The potential vorticities evolve as

$$\frac{D_{\mathrm{BT}}}{Dt}q_{\mathrm{BT}} = -J(\psi_{\mathrm{bc}}, q_{\mathrm{bc}}) - \frac{r}{2}(\zeta_{\mathrm{BT}} - \zeta_{\mathrm{bc}}), \tag{5}$$

$$\frac{D_{\mathrm{BT}}}{Dt}q_{\mathrm{bc}} = -J(\psi_{\mathrm{bc}}, q_{\mathrm{BT}}) + \frac{r}{2}(\zeta_{\mathrm{BT}} - \zeta_{\mathrm{bc}}) - f_0\frac{S}{H}. \tag{6}$$

For the classic two-layer QG model, $S = 0$, in which case Eqs. (5) and (6) are a closed set of equations for two quantities which, in absence of dissipation ($r = 0$), are conserved in the domain average. The inclusion of diabatic forcing terms disrupts this conservation.

b. Incorporating moisture

Moisture introduces latent heat release to the diabatic forcing term S. This requires an equation for water content. We assume that the mixing ratio of water is close to a reference value m_0. We introduce a *thickness equivalent* mixing ratio m—with units of height—such that the total mixing ratio is $m_0(1 + m/H)$. Since the lower atmosphere contains the bulk of the moisture content, this weighted mixing ratio is defined only in the bottom layer of the system. It is continuously replenished by evaporation of water from the surface at rate E, which we will hold constant. The water budget can be written as

$$\frac{D_{\mathrm{BT}}}{Dt}m = J(\psi_{\mathrm{bc}}, m) + W - P + E. \tag{7}$$

Hence moisture is transported by the lower-level flow (here decomposed into barotropic and baroclinic components), removed by precipitation P, replenished by surface evaporation E, and increased by low-level convergence W.

Water vapor condenses when the value of m exceeds a saturation value m_s set by the Clausius–Clapeyron relation, here represented by a linearization with respect to temperature perturbation η:

$$m_s = \mathcal{C}\eta = 2\mathcal{C}\frac{\lambda^{-2}H}{f_0}\psi_{\mathrm{bc}}, \tag{8}$$

with $\mathcal{C}$ the gradient of Clausius–Clapeyron with respect to temperature perturbation. At points where the mixing ratio exceeds this value—where the system becomes supersaturated—precipitation relaxes the mixing ratio down to the saturation value with characteristic time τ, such that

$$P = \begin{cases} (m - m_s)/\tau = (m - \mathcal{C}\eta)/\tau & \text{where } m > m_s \\ 0 & \text{where } m \le m_s \end{cases}. \tag{9}$$

The diabatic forcing in Eq. (4) consists of the combined effects of latent heat release and radiative cooling. Following the formulation of Lapeyre and Held (2004), we will define the total diabatic forcing as

$$S \equiv \mathcal{L}(P - E), \tag{10}$$

with

$$\mathcal{L} \equiv \frac{L_q m_0}{c_p \delta\theta} \in [0, 1). \tag{11}$$

Here, L_q is the latent heat of vaporization, m_0 the reference mixing ratio, and $c_p\delta\theta$ dry stratification, and $\mathcal{L}E = R$, the radiative cooling, with $\mathcal{L}$ being the moisture stratification of the system, characterizing the ratio of available latent heat to sensible heat loss as a parcel ascends adiabatically. In the limit $\mathcal{L} \to 1$, the available latent heat can fully compensate for the adiabatic cooling of a parcel as it ascends, thereby contradicting the assumption of stratification.

c. *Moist potential vorticity*

In the dry QG system, the interface η and baroclinic vorticity $\zeta_{\rm bc}$ exchange energy through vertical motion W with a constant ratio of f_0/H. The baroclinic PV can be thought of as the vorticity after the thickness perturbation is brought back to 0, so that the thickness perturbation to the (dry) PV is $-f_0\eta/H$. In this sense, the thickness acts as the "reservoir" available for conversion into baroclinic vorticity. In the moist case, precipitation contributes to the thickness reservoir. This contribution can be characterized by a second reservoir, defined by combining Eqs. (4) and (7) to eliminate the vertical motion W and isolate the precipitation tendency, e.g.,

$$\eta_c = \eta + \frac{m - m_s}{1 + \mathcal{C}}, \tag{12}$$

which evolves as

$$\frac{D_{\rm BT}}{Dt}\eta_c = J(\psi_{\rm bc}, \eta_c) - \frac{\mathcal{L}(P - E)}{\mu_s - 1}. \tag{13}$$

The quantity

$$\mu_s = \frac{1 + \mathcal{C}\mathcal{L}}{1 - \mathcal{L}} \tag{14}$$

characterizes the reduction to the static stability associated with moist effects. A key feature of this reservoir is its conservation in the absence of adiabatic forcings, including precipitation, evaporation, radiative cooling, and dissipative effects. At saturation, $m = m_s$ and $\eta_c = \eta$. We propose interpreting η_c as the condensation level. Indeed, noting that moisture is confined below the height set by the interface value η, the condensation trigger can be visualized as the condition that the interface rises above the condensation level, as depicted in Fig. 2.

Vertical motions then resolve anomalies in the term

$$\eta + (\mu_s - 1)\eta_c = \frac{\eta + \mathcal{L}m}{1 - \mathcal{L}}, \tag{15}$$

which resembles the moist static energy with a rescaling relating to the moisture stratification. By analogy with the dry model, this quantity can be thought of as a reservoir of baroclinic vorticity that can be converted through vertical motion. When precipitation is the dominant forcing impacting η_c, this reservoir is enhanced through a combination of two effects: first, it includes a contribution from the moisture field in addition to the thickness perturbation; second, the impact of vertical velocity is reduced by a factor $1 - \mathcal{L} < 1$. Moist baroclinic PV (MPV) can be conceptualized as the baroclinic vorticity after the perturbation to the *total effective reservoir* is brought back to zero by vertical motion. This yields a *moist baroclinic potential vorticity* of the form

$$q_m = \zeta_{\rm bc} - \frac{f_0}{H}[\eta + (\mu_s - 1)\eta_c]. \tag{16}$$

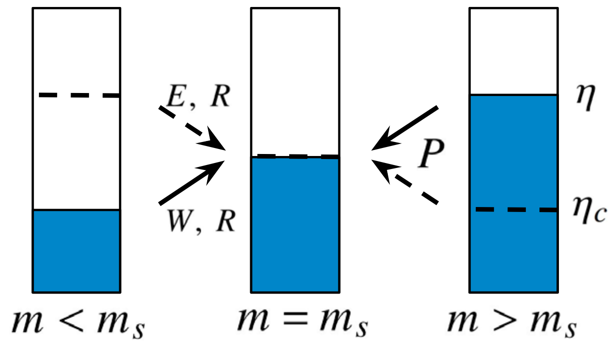

FIG. 2. A schematic for the condensation level η_c as a metric for saturation. When the interface η between the top (white) and bottom (blue) layers is below the condensation level η_c, the system is subsaturated. The interface η evolves by dynamical processes and radiative cooling R, while the condensation level η_c evolves with competing effects from evaporation E and radiative cooling R. When η rises above η_c, precipitation P quickly acts to bring the two to parity by removing water vapor and lowering the interface.

This is a baroclinic formulation based on the MPV derived in Lapeyre and Held (2004), and also resembles the gross PV of Adames and Ming (2018) and Adames (2021). Its evolution equation is given by

$$\frac{D_{\rm BT}}{Dt}q_m = -J\left[\psi_{\rm bc}, q_{\rm BT} + \frac{f_0}{H}(\mu_s - 1)\eta_c\right] + \frac{r}{2}(\zeta_{\rm BT} - \zeta_{\rm bc}). \tag{17}$$

The parameter μ_s plays a central role in the MQG system. It characterizes a reduction to the effective static stability of the atmosphere as a result of precipitation (Neelin and Held 1987; Emanuel et al. 1994; Adames 2021): the larger μ_s, the lower the effective stratification. Similar parameters have been shown to relate to the efficiency of precipitation as a dehumidification process (Inoue and Back 2015, 2017). A connection between Eq. (13) and the wet-bulb temperature equation of Pauluis et al. (2008) can be achieved by taking $1 - \mu_s^{-1}$ to be the moisture stratification of the system. Crucially, their implementation does not include a Clausius–Clapeyron relation, which introduces interactions between temperature and moisture, including in the horizontal gradient and the preferential latent heat release in warm sectors of the atmosphere. In particular, a nonzero $\mathcal{C}$ increases precipitation in regions where low-level convergence shifts the interface upward. Because precipitation has an opposite effect to positive W, increasing $\mathcal{C}$ decreases the efficiency of upward motions in removing temperature anomalies.

d. *The saturated limit*

The nonlinearity of the precipitation trigger (9) introduces a major complication in the study of moist turbulent dynamics. This nonlinearity, however, is absent in two limiting scenarios: a dry atmosphere with no precipitation, and a fully saturated atmosphere with precipitation everywhere. While the first scenario has been well documented, we argue here that the second scenario, which we refer here to as the saturated limit, can offer additional insights on the impacts of moisture on geostrophic turbulence.

The saturated limit can be achieved if one makes the assumption that precipitation acts quickly enough to maintain the system near saturation. Within the MQG system described above, the limit of complete saturation can be nearly achieved by increasing the evaporation parameter E and decreasing the precipitation relaxation scale τ. The former increases the amount of water vapor added to the system at every time step, ensuring at sufficiently high values that the system is never subsaturated. The latter decreases the amount of time that the system takes to relax to the saturated value, decreasing the value of the moisture surplus $m = m_s$ in a supersaturated system. Applying both of these limits corresponds to the strict quasi-equilibrium approximation of Emanuel et al. (1994).

Mathematically, the saturated limit amounts to enforcing the condition that the moisture is equal to its saturation value, i.e., $m = m_s = C\eta$, or equivalently that the condensation level is equal to the interface position, i.e., $\eta_c = \eta$. As a result, the MPV can be written as

$$q_{\rm ms} = \zeta_{\rm bc} - \mu_s \frac{f_0}{H}\eta = \zeta_{\rm bc} - \mu_s \lambda^{-2}\psi_{\rm bc}. \tag{18}$$

This is similar to the expression for the baroclinic PV, but with the deformation radius rescaled by a factor $\mu_s^{-1/2}$. Furthermore, the MPV Eq. (17) becomes

$$\frac{D_{\rm BT}}{Dt}q_{\rm ms} = -J(\psi_{\rm bc}, q_{\rm BT}) + \frac{r}{2}(\zeta_{\rm BT} - \zeta_{\rm bc}). \tag{19}$$

Appendix A demonstrates that the saturated limit is equivalent to the dry if one substitutes the MPV for the dry and makes appropriate modifications to characteristic length and time scales. Thus, the saturated limit is expected to behave similarly to class two-layer QG turbulence, and will be the focus of the scaling arguments in section 5.

3. Numerical simulations

The atmosphere has a meridional temperature forcing associated with incoming solar radiation. To capture this effect, we prescribe a linear background gradient and model the evolution of the perturbation, denoted with a prime. The baroclinic streamfunction is prescribed a mean background gradient $\Psi_{\rm bc} = -U/2y$, associated with an externally forced temperature gradient. The total baroclinic streamfunction is $\psi_{\rm bc} = \Psi_{\rm bc} + \psi'_{\rm bc}$, with the prime denoting a perturbation. Since the baroclinic streamfunction has a background gradient, the interface also has a reference state $\overline{\eta} = -UHy/\lambda^2 f_0$. Correspondingly, the barotropic and baroclinic PV have mean gradients $Q_{\rm BT} = \beta y$ and $Q_{\rm bc} = Uy/\lambda^2$. In the dry case, instability occurs when the mean baroclinic PV gradient is larger than the gradient of the Coriolis parameter. This can be recast in terms of the criticality ξ as

$$\xi = \frac{U}{\beta\lambda^2} > 1. \tag{20}$$

The mixing ratio has a meridional gradient associated with the temperature gradient, with higher moisture content near the equator than the poles. The moisture content preferentially adjusts toward the saturation value associated with the local temperature, with precipitation relaxing supersaturated regions toward the saturation value and while evaporation increases the moisture content globally. The reference state of the mixing ratio can be set by combining Eq. (8) with the reference state of the temperature, yielding the background gradient $M = \mathcal{C}\overline{\eta} = -\mathcal{C}UH/\lambda^2 f_0 y$. The MPV has background gradient $Q_m = \mu_s U\lambda^{-2}y$. Last, the implementation of precipitation requires a closure to account for strict nonnegativity. We follow the closure of Lapeyre and Held (2004), described in appendix C.

We perform experiments on a doubly periodic domain in spectral space with a 256 × 256 grid, The domain size L is chosen such that $2\pi\lambda = L/9$. Simulations were run for a time $T = 400\lambda/U$. Time averages are computed over the last half of the run with sampling at intervals of $\delta t = 0.1\lambda/U$. Time stepping uses a third-order Adams–Bashforth method with an integrating factor to remove the stiff portion of the equation and the Jacobian handled pseudospectrally with antialiasing. Time stepping is done for the upper ($q_{\rm BT} + q_{\rm bc}$), lower ($q_{\rm BT} - q_{\rm bc}$), and moist lower ($q_{\rm BT} - q_m$) PV, thereby eliminating the need to compute the vertical motion W. The upper and lower streamfunctions are computed diagnostically in Fourier space. Precipitation is computed diagnostically in real space from the moisture surplus, $(m - m_s)/(1 + \mathcal{C}) = \lambda^2(q_m - q_{\rm bc}) + (\mu_s - 1)\psi_{\rm bc}$.

The simulations used for data in this paper span the parameter space listed in the right column of Table 2. Realistic values are listed in column 3. The estimate for the precipitation relaxation time scale τ^* comes from analyses of the tropics, which suggest time scales from 2 (Betts and Miller 1986) to 12 h (Bretherton et al. 2004). The rationale for all other physical parameters can be found in Lapeyre and Held (2004). The time step was chosen based on the stability of the simulation. The eighth-order hyperdiffusion coefficient ν^* was chosen to allow for dissipation at small scales without suppressing the smaller-scale instability associated with latent heat release.

Figure 3 displays snapshots of the barotropic vorticity (first column), baroclinic PV (second column), and MPV (third column) in three of these simulations. The first row shows a dry simulation ($\mu_s = 1$) at supercriticality $\xi = 1.25$. As the configuration is only slightly supercritical, the flow is only weakly unstable and is organized in six fairly narrow zonal jets. The second row shows a moist simulation with $\mu_s = 4.0$ at the same dry criticality $\xi = 1.25$. An intensification of the flow is evidenced by the increase in the magnitude of the vorticity anomalies. The range of motions is substantially enhanced both at small scales, with the emergence of closed vortices, and at large scale with the organization of the flow around two zonal jets instead of six. Finally, the third row shows a dry simulation ($\mu_s = 1.0$), but at criticality $\xi = 5$. This supercriticality is chosen as to match the value of $\mu_s\xi$ in the simulation shown in the second row. Qualitatively, the simulations in the second and third rows exhibit similar levels of turbulence, albeit with systematically larger scale of motions in the dry simulation.

TABLE 2. Tunable parameter space (nondimensionalized), realistic values, and the values used in the simulations here. To enforce the saturated limit, the integrations were done with a very large value of the evaporation $\mathcal{E}$ and a very small precipitation relaxation time scale τ^*.

Parameter	Expression	Realistic	Represents	Simulation values
ξ	$\frac{U}{\beta\lambda^2}$	1	Dry criticality	0.8, 1.0, 1.25
$\mathcal{R}$	$\frac{r\lambda}{U}$	0.16	Ekman damping	0.16
$\mathcal{L}$	$\frac{Lm_0}{c_p\delta\Theta}$	0.2–0.35	Vertical moisture stratification	0.0, 0.1, 0.2, 0.3, 0.4, 0.5, 0.6, 0.7
$\mathcal{C}$	$\mathcal{C}$	2	Clausius–Clapeyron effects	0.0, 2.0
$\mathcal{E}$	$\frac{Ef_0\lambda^2}{U^2m_0}$	0.4	Moisture uptake	1000
τ^*	$\frac{\tau U}{\lambda}$	<0.15–0.85	Precipitation time scale	0.001 25
L/λ	L/λ	—	Domain size	18π
dt	$\frac{\Delta t U}{\lambda}$	—	Time step	0.000 25
ν^*	$U\lambda^7\nu$	—	Small-scale dissipation	10^{-7}

To better quantify the turbulence, Fig. 4 displays the time-averaged eddy kinetic energy (EKE) spectra for the barotropic and baroclinic modes. These energies are defined in section 4. We observe an increase in the barotropic EKE of roughly a factor of 100 from the $\mu_s = 1.0$ case to the $\mu_s = 4.0$ case in for simulations with $\xi = 1.25$ and $\xi = 0.8$. There is a corresponding shift to larger scales of the Rhines scale k_0, defined by

$$k_0 = \sqrt{\frac{\beta}{V}}, \tag{21}$$

where V is the root-mean-square barotropic velocity. This scale provides an estimate for the termination of the inverse cascade.

For the same change in μ_s, the peak of the baroclinic EKE for both values of the dry criticality ξ increases by roughly a factor of 2 and shifts to smaller scales. We approximate the location of this peak by a centroid of the baroclinic EKE, given by

$$\overline{K}_{\rm bc} = \left(\frac{\int K^2 \mathrm{EKE}_{\rm bc} dK}{\int \mathrm{EKE}_{\rm bc} dK}\right)^{1/2}. \tag{22}$$

The relative increase of the barotropic and baroclinic energy is such that the peaks are roughly equal in the least energetic simulation ($\xi = 0.8$, $\mu_s = 1.0$) and roughly two orders of magnitudes different in the most energetic simulations. Indeed, the dry system is predicted to be subcritical when $\xi = 0.8$, but exhibits supercritical growth at large μ_s. These scale changes are what we seek to explain in the remainder of this paper.

4. Energetics

The MQG system exhibits features across a broad range of scales. Held and Larichev (1996) argue that the energetics of the (dry) QG system can be understood as an inverse energy cascade associated with barotropic motions, and a direct cascade of APE. The two cascades are coupled in the sense that the APE is mixed to smaller scales by the barotropic flow before being converted into kinetic energy, which in turn sustains the cascade of barotropic kinetic energy to large scales. We revisit how the inclusion of moist processes modifies this picture by quantifying an additional source of energy associated with the poleward transport of moisture.

In the classical two-layer QG system, the energetics can be decomposed into barotropic and baroclinic components. The barotropic energy is purely a kinetic energy term constructed as $\mathrm{EKE}_{\rm BT} = |\nabla\psi'_{\rm BT}|^2/2$. Its evolution in the domain average can be constructed from Eq. (1) as

$$\partial_t \overline{\mathrm{EKE}}_{\rm BT} = \mathcal{B} - \mathcal{D}_{\rm BT}. \tag{23}$$

Here, the overline indicates a domain average. The barotropic energy equation is unchanged from the dry QG case. It receives injections of energy from the baroclinic mode $\mathcal{B} = \overline{\psi'_{\rm BT} J(\psi'_{\rm bc} - U/2y, \nabla^2\psi'_{\rm bc})}$ and dissipates via an Ekman term $\mathcal{D}_{\rm BT} = r\overline{\nabla\psi'_{\rm BT} \cdot \nabla(\psi'_{\rm BT} - \psi'_{\rm bc})/2}$. The Ekman term also introduces an interaction between the barotropic and baroclinic modes; however, this is small compared to the barotropic dissipation and will be disregarded.

The baroclinic energy $E_{\rm bc}$ consists of a kinetic energy component $\mathrm{EKE}_{\rm bc} = |\nabla\psi'_{\rm bc}|^2/2$ and an available potential energy component APE $= g^*\eta'^2/(4H)$. In the domain average, its evolution can be computed from the baroclinic PV as

$$\partial_t \overline{E_{\rm bc}} = -\mathcal{B} - \mathcal{D}_{\rm bc} + \varepsilon_{\rm APE} + \mathcal{P}. \tag{24}$$

The baroclinic energy equation differs from its dry counterpart only in the inclusion of a precipitation term $\mathcal{P} = g^*\mathcal{L}\overline{P'\eta'}/(2H)$. This characterizes the generation of APE due to latent heat

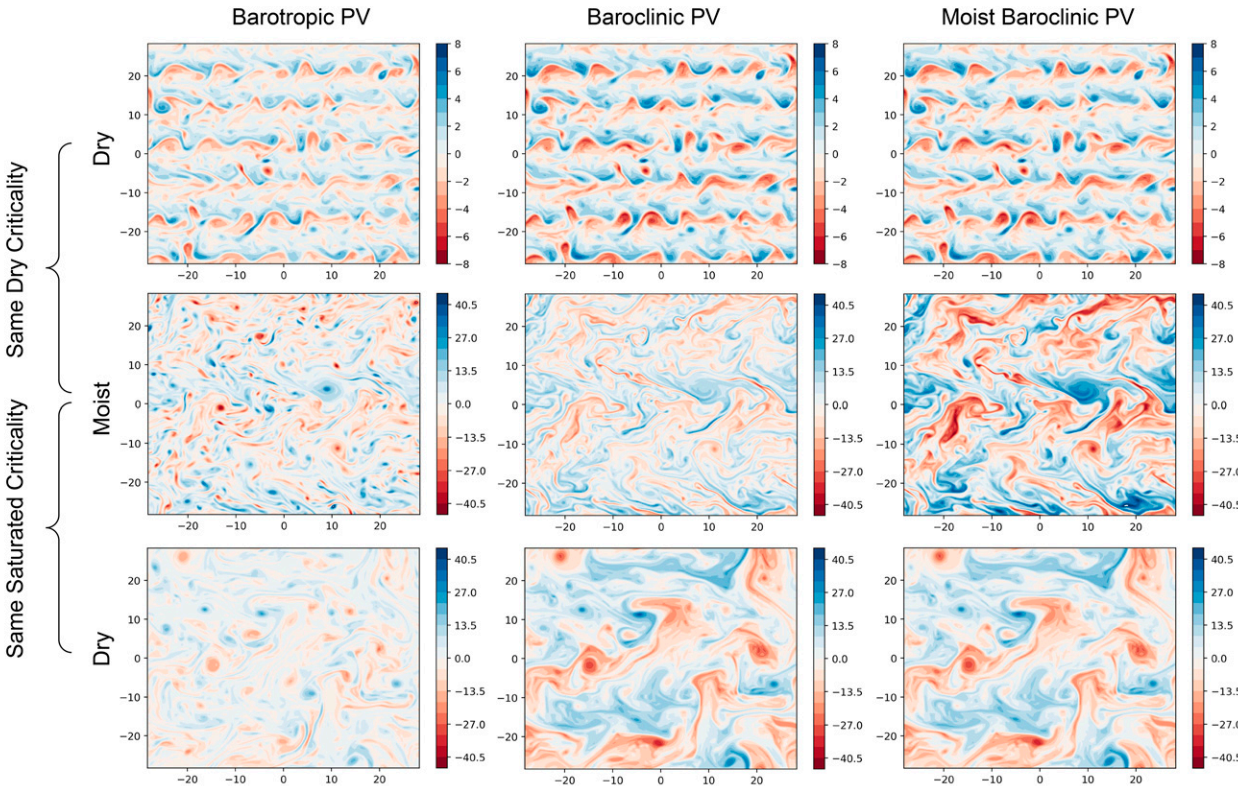

FIG. 3. Snapshots of the barotropic, baroclinic, and moist baroclinic potential vorticity perturbation for three cases. (top) A dry case with mild supercriticality ($\xi = 1.25$, $\mu_s = 1.0$). (middle) A saturated case with the same dry criticality as the first case and moisture ($\xi = 1.25$, $\mu_s = 4.0$). (bottom) Another dry case with higher criticality ($\xi = 5.0$, $\mu_s = 1.0$), chosen so that the second and third cases have same total saturated criticality. Both exhibit more energetic flows than the top row; note the change in color scale. The middle row, as the only moist system, is the only row to exhibit a smaller magnitude of (center) dry baroclinic PV compared to (right) the moist. This is associated with the inclusion of moisture in the "reservoir" for conversion into baroclinic vorticity. Additionally, the middle row is dominated by small-scale vorticity, consistent with a shift to smaller scales, in contrast with the bottom row with the same saturated criticality.

release. The first term is the transfer from the baroclinic to the barotropic mode as described above, and the Ekman term $\mathcal{D}_{\rm bc} = r\overline{\nabla\psi'_{\rm bc}\cdot\nabla(\psi'_{\rm BT}-\psi'_{\rm bc})/2}$ dissipates kinetic energy, similar to the corresponding term in the barotropic equation. The APE is generated by a downgradient flux of sensible heat $\varepsilon_{\rm APE} = -g^*\overline{\eta}_y\overline{\upsilon'_{\rm BT}\eta'}/(2H)$ that acts as a source of baroclinic energy at small scales.

Precipitation acts as a conversion term between ME and baroclinic energy, while total energy—defined as the sum of its barotropic, baroclinic, and moist components—is conserved. To capture the source of this injection into the baroclinic energy, we define ME as

$$\mathrm{ME} = \frac{g^*}{4H}(\mu_s - 1)\eta'^2_c. \tag{25}$$

By multiplying Eq. (13) by $(\mu_s - 1)\eta'_c$ and taking a domain average, we obtain that the domain average $\overline{\mathrm{ME}}$ evolves as

$$\partial_t\overline{\mathrm{ME}} = \varepsilon_{\rm ME} - \mathcal{P} - \mathcal{D}_P. \tag{26}$$

The first term captures the generation of ME, with further elaboration below. The second term, defined in the context of Eq. (24) captures the transfer from ME to APE by precipitation. The third captures the dissipation of ME due to precipitation $\mathcal{D}_P = (g^*H/2)[\mathcal{L}/(1+\mathcal{C})]\tau\overline{P'^2}$, which vanishes in the limit $\tau \to 0$. Since this limit is an assumption of strict quasi equilibrium, the third term will be neglected. The generation of ME can be written as

$$\varepsilon_{\rm ME} = -\frac{g^*}{2H}(\mu_s - 1)\overline{\eta}_y\overline{(\upsilon'_{\rm BT} - \upsilon'_{\rm bc})\eta'_c}. \tag{27}$$

This shows that a downgradient transport of the condensation level acts as a source of ME. It results from a combination of a downgradient thickness and humidity transports. In the saturated limit, the two are related and the generation of ME is proportional to the downgradient thickness flux:

$$\varepsilon_{{\rm ME},s} = -\frac{g^*}{2H}(\mu_s - 1)\overline{\eta}_y\overline{\upsilon'_{\rm BT}\eta'}. \tag{28}$$

We can then combine Eqs. (24) and (26) to create a budget for the total moist baroclinic energy $E_{\rm mb}$:

$$\partial_t\overline{E_{\rm mb}} = -\mathcal{B} - \mathcal{D}_{\rm bc} + \varepsilon_{\rm APE} + \varepsilon_{\rm ME}. \tag{29}$$

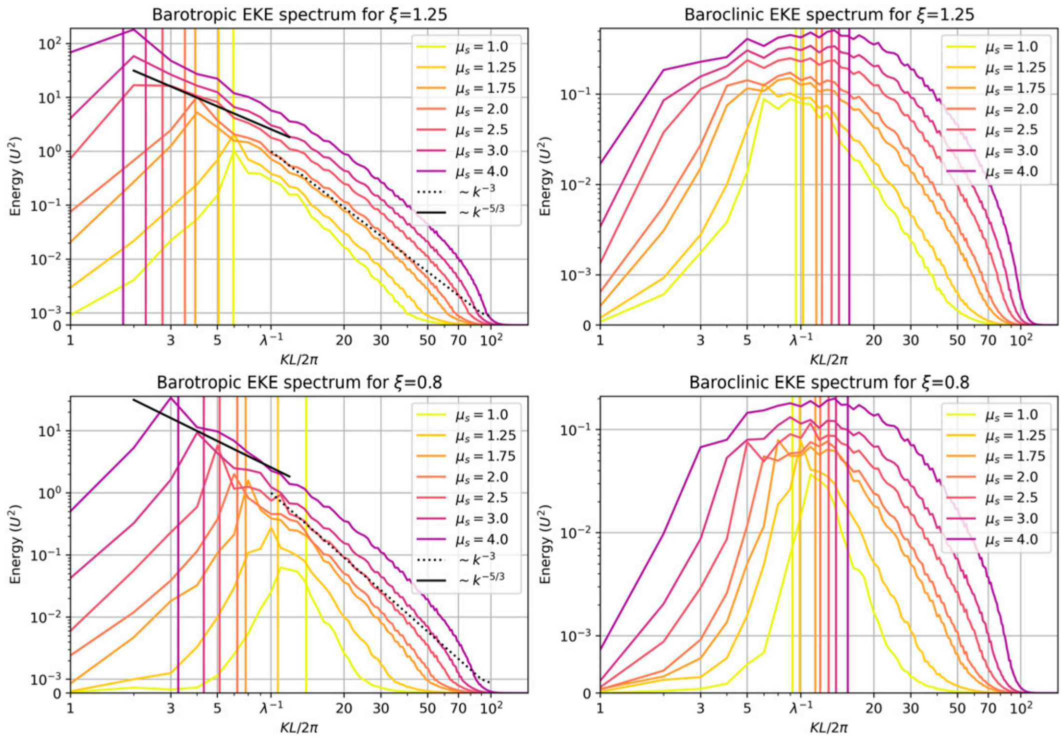

FIG. 4. Spectra of the barotropic and baroclinic eddy kinetic energy for a few values of μ_s with (top) $\xi = 1.25$ and (bottom) $\xi = 0.8$. The horizontal scale is the wavelength rescaled by the largest wavelength $2\pi/L$, where L is the domain size. The y axis is plotted in symlog scale, such that the figures are linear for values smaller than 10^{-4} and log scale for larger values. The vertical lines in the barotropic mode are the Rhines scale, associated with the termination of the inverse cascade. The vertical lines in baroclinic mode mark the centroid of the baroclinic eddy kinetic energy.

The total energy generation of the system can then be computed as $\varepsilon = \varepsilon_{\rm APE} + \varepsilon_{\rm ME}$, which at saturation can be estimated as

$$\varepsilon = \varepsilon_{\rm APE} + \varepsilon_{\rm ME} \approx -\mu_s \frac{g^*}{2H}\overline{\eta}_y \overline{v'_{\rm BT}\eta'}, \tag{30}$$

with corresponding dissipation

$$\mathcal{D} = \frac{r}{2}\overline{|\nabla(\psi'_{\rm BT} - \psi'_{\rm bc})|^2}. \tag{31}$$

The energy transfer for moist geostrophic turbulence in the saturated limit is depicted in Fig. 5. The meridional transport of sensible and latent heat acts as energy sources for APE ($\varepsilon_{\rm APE}$) and ME ($\varepsilon_{\rm ME}$). In the limit of short adjustment time, the dissipation of ME by precipitation is negligible $\mathcal{D}_P \sim 0$, so that ME is fully converted into baroclinic energy by precipitation ($\mathcal{P}$). In addition, as with traditional (dry) geostrophic turbulence, baroclinic energy is converted into baroclinic energy ($\mathcal{B}$), while kinetic energy is lost due to surface friction ($\mathcal{D}_B$ and $\mathcal{D}_b$).

If one assumes that the atmosphere is in statistical equilibrium, there must be a balance between the generation and the dissipation of energy over long time scales. In the saturated limit, all of the total injection into the barotropic mode is balanced by the amount of moist available potential energy (MAPE = APE + ME) generated. Hence,

$$\begin{aligned} \frac{\langle \varepsilon_{\rm APE}\rangle + \langle \varepsilon_{\rm ME}\rangle}{\langle \mathcal{D}\rangle} &= 1, \\ \frac{\langle \varepsilon_{\rm APE}\rangle + \langle \varepsilon_{\rm ME}\rangle}{\langle B\rangle} &= 1, \end{aligned} \tag{32}$$

where the angle brackets indicate a sufficiently long time average. Figures 6a and 6b demonstrate that both of these assumptions hold up well in our simulations and may be used for scaling arguments. The system is in statistical equilibrium, and ε can be used to estimate the barotropic energy injection $\mathcal{B}$.

Statistical averages also predict the conversion rate of ME into precipitation and the relative contribution of APE and ME generation to the total energy. For the saturated limit,

$$\begin{aligned} \frac{\langle \mathcal{P}\rangle}{\langle \varepsilon_{\rm ME}\rangle} &= 1, \\ \frac{\langle \varepsilon_{\rm ME}\rangle}{\langle \varepsilon_{\rm APE}\rangle} &= \mu_s - 1, \\ \frac{\langle \mathcal{P}\rangle}{\langle \varepsilon_{\rm APE}\rangle} &= \mu_s - 1. \end{aligned} \tag{33}$$

Figures 6c and 6d demonstrates that the saturated system efficiently converts ME into precipitation. As such, the precipitation $\mathcal{P}$ can be estimated by $\varepsilon_{\rm ME}$ and vice versa. At higher values of μ_s, less energy is generated from precipitation than

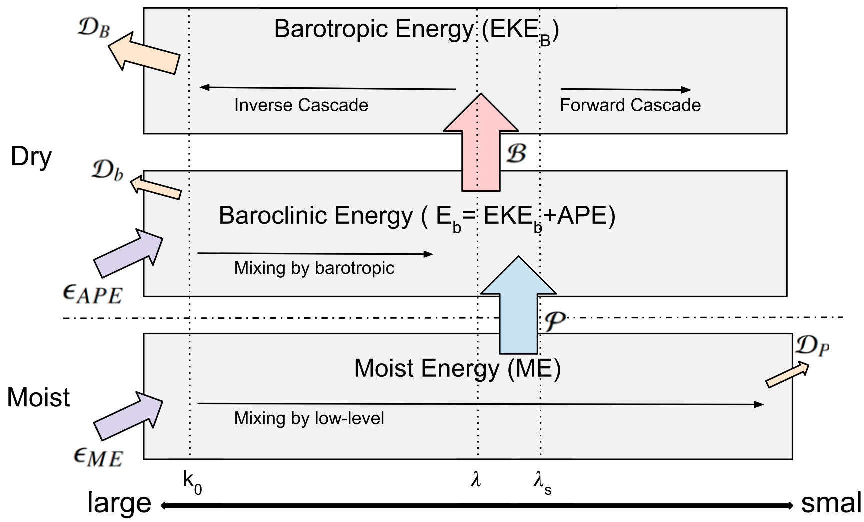

FIG. 5. Energy transfers in the MQG model, with the estimates of the scaling at saturation. At large scales, the background moisture and temperature gradients are redistributed by the barotropic flow, acting as a source for the APE and ME, $\varepsilon_{\mathrm{APE}}$ and $\varepsilon_{\mathrm{ME}}$, respectively (purple arrows). The energy is mixed to smaller scales by the barotropic flow until near the Rossby radius. The precipitation $\mathcal{P}$ (blue arrow) transfers ME into APE across, with a peak near the saturated Rossby radius. The baroclinic mode injects energy into the barotropic $\mathcal{B}$ (red arrow). The barotropic flow has an inverse energy cascade to larger scales and a forward enstrophy cascade to smaller scales. Dissipation (orange arrows) occurs primarily through Ekman dissipation of the barotropic mode $\mathcal{D}_{\mathrm{BT}}$ at large scales. Additional dissipation occurs with Ekman dissipation of the baroclinic mode $\mathcal{D}_{\mathrm{bc}}$ at large scales and precipitation dissipation $\mathcal{D}_P$ mostly at small scales. Additional hyperdiffusion occurs in all modes, but can be neglected and is not depicted here.

predicted at saturation. However, more subsaturated points occur in the simulations with high μ_s, so it is possible that this deficit is due to an increased portion of the domain at subsaturation. This also explains the small deficit in barotropic energy generation at large μ_s. The ratio of precipitation to sensible heat flux scales as $\mu - 1$, as predicted. Notably, the sensible heat flux is the dominant contribution to APE for $\mu_s < 2$, while precipitation dominates for $\mu_s > 2$. This is consistent with a shift from a sensible heating to a latent heating dominated regime, which points to a change in growth mechanism such as described in Parker and Thorpe (1995), de Vries et al. (2010), and Adames (2021).

5. Scalings

The previous section argues that geostrophic turbulence is characterized by the generation, conversion and dissipation of three different components of the energy budget. Here, we focus on the scales at which these occur. Scaling arguments for the termination of the inverse cascade (e.g., Held and Larichev 1996) often assume that the system has an inertial range: a sufficient scale separation between the injection scale and dissipation scale. In practice, such scaling arguments still offer useful insights, even in the absence of a clear inertial range.

a. Linear stability analysis

We will begin with a linear stability analysis, similar to those done in greater detail by de Vries et al. (2010), Adames and Ming (2018), and Adames (2021), among others. Recall that, in the dry case, instability occurs when there is a sign reversal in the total PV gradient. In the two-layer case, this requires that the mean baroclinic PV gradient be larger than the gradient of the Coriolis parameter. Similarly, in the saturated limit, instability occurs when the *mean MPV gradient* is larger than the gradient of the Coriolis parameter, or, expressed in terms of a saturated criticality ξ_s,

$$\xi_s \equiv \frac{\mu_s U}{\beta \lambda^2} \equiv \mu_s \xi \geq 1, \tag{34}$$

where ξ is the dry criticality. As $\mu_s \geq 1$ (equality holding only in the dry limit), the saturated criticality $\xi_s \geq \xi$. In particular, it is possible for the saturated system to be unstable with $\xi_s > 1$, even where the classical dry theory would predict stability, $\xi < 1$.

Figure 3 shows that the scalings of moist systems cannot be determined by ξ or ξ_s alone. The top and middle rows depict the potential vorticities of a dry and moist simulation with the same value of ξ, demonstrating the increase in energy at both small and large scales associated with the inclusion of moisture. The middle and bottom rows depict the potential vorticities of a moist and dry simulation with the same value of ξ_s, demonstrating that the moist system exhibits smaller-scale vortices than the dry with equivalent moist criticality.

Figure 7 shows the linear growth rate σ as function of the wavenumber modulus K and λ. As with previous equations in

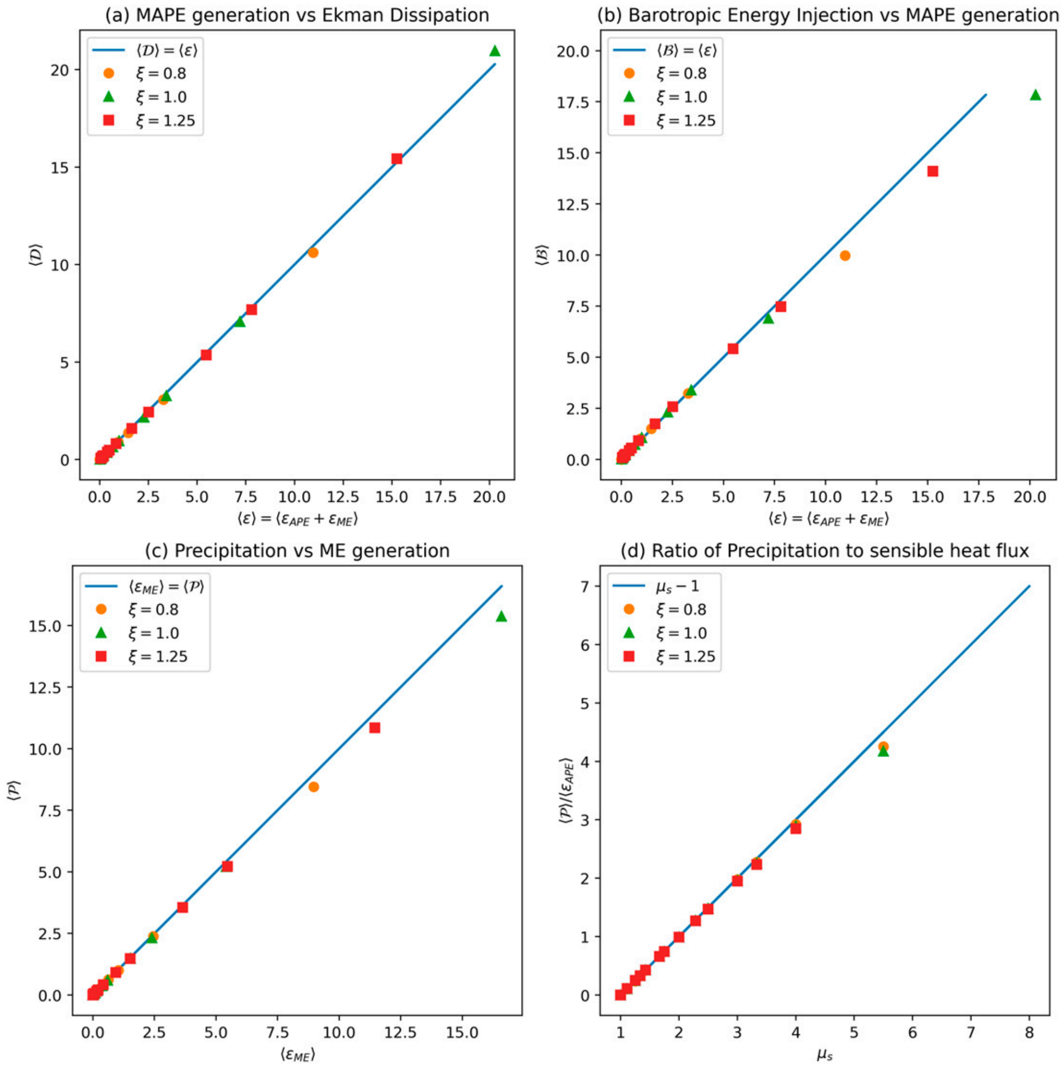

FIG. 6. The balance of (a) the total generation of energy vs the Ekman dissipation, (b) the generation of MAPE vs the injection into barotropic energy, (c) the generation of ME and conversion to precipitation, and (d) the ratio of precipitation injection to sensible heat flux, the two contributions to the generation of APE.

the saturated linear instability analysis, the linear growth rate matches the expression for the classic two-layer baroclinic instability, with the saturated versions of criticality and a saturated Rossby deformation radius $\lambda_s = \mu_s^{-1/2}\lambda$ replacing their dry counterparts,

$$\sigma = \frac{Uk}{(\lambda_s K)^4 + 2(\lambda_s K)^2}\left[\frac{(\lambda_s K)^8}{4} - (\lambda_s K)^4 + \xi_s^{-2}\right]^{1/2}, \qquad (35)$$

where k is the wavenumber corresponding to propagation in the x (zonal) direction. Figure 7 considers the case with $K = k$.

The saturated limit also implies changes in the spectrum of unstable modes, which are confined between lower and upper wavenumber moduli K_- and K_+, defined by

$$K_\pm^4 = 2\mu_s^2\lambda^{-4}\left(1 \pm \sqrt{1 - \mu_s^{-2}\xi^{-2}}\right). \qquad (36)$$

The impact of the moist parameter μ_s is twofold: the spectrum tends toward higher wavenumber, and the range of unstable modes increases.

It is convenient to consider the limit of strong supercriticality ($\xi_s \gg 1$), in which case the long- and shortwave cutoff can be written as

$$K_-\lambda \approx \xi^{-1/2}, \qquad (37)$$

$$K_+\lambda \approx 2^{1/2}\mu_s^{1/2}. \qquad (38)$$

Figure 7 illustrates these asymptotic limits. While the longwave cutoff K_- exhibits little dependency on μ_s, the shortwave cutoff K_+ shifts to smaller scales. The latter change was found in Adames (2021) in the limit of instantaneous precipitation relaxation. Consequently, the spectrum of unstable modes broadens with increasing μ_s. Because Eq. (35) is equivalent to

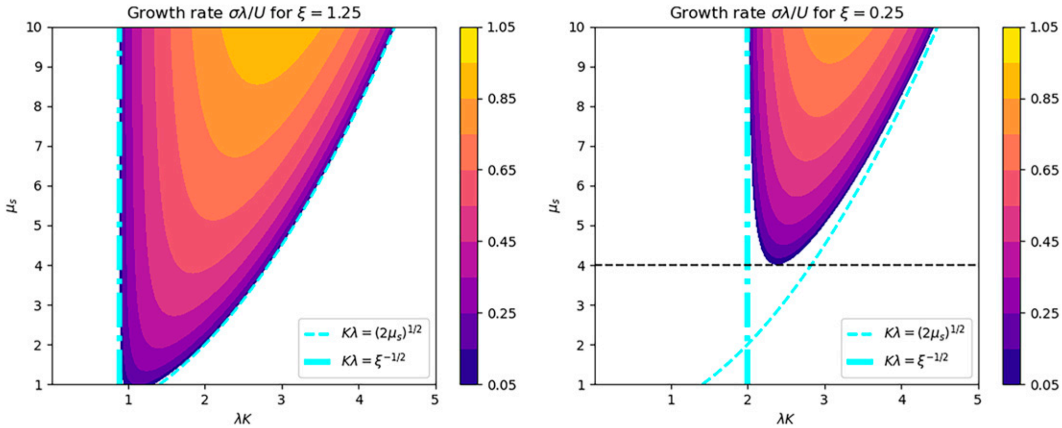

FIG. 7. Growth rate as a function of scale $K\lambda = |k|\lambda$ and the gross moisture stratification μ_s, with dry criticality ξ fixed as the value indicated in each title. (right) The dashed horizontal line corresponds to the value of μ_s necessary to achieve marginal saturated criticality. The two lines enveloping the contour correspond to asymptotic bounds on the unstable region in the limit $\xi_s \to \infty$.

the growth rate of the dry system under rescaling, we can predict that when ξ_s is held constant, the unstable modes will shift to smaller scales as $\mu_s^{1/2}$ and the fastest growth rate will increase as $\mu_s^{1/2}$.

We return to Fig. 3 to see how well these predictions play out. The simulations depicted in the middle and bottom rows have equal values of ξ_s. However, the middle row has $\mu_s = 4.0$, while the bottom row is dry. The results of the linear stability analysis predict instability on a length scale that is a factor $\mu_s^{1/2} = 0.5$ smaller in the middle row compared to the bottom row. Indeed, we observe a roughly factor of 2 change in the scale of vortices between the two integrations.

b. Baroclinic energy

Baroclinic energy is generated through the downgradient transport of sensible heat $\varepsilon_{\mathrm{APE}}$ and through precipitation $\mathcal{P}$. Figure 8a captures the total injection into the APE. The peak injection increases by nearly a factor of 100 and broadens to both smaller and larger scales as μ_s increases. The energy injection can be decomposed into the sensible heat flux and the precipitation injection. Figure 8b shows the sensible heat flux increasing across all scales, with the peak shifting to larger scales with increasing μ_s. In contrast, as shown in Fig. 8c, precipitation generates APE at smaller scales as μ_s increases. The broadening shown in Fig. 8a arises with a combination of the dry and moist injections, which dominate at large and small scales, respectively.

For large μ_s, there is a small but noteworthy removal of APE by precipitation at large scale. As in Bembenek et al. (2020) and Lutsko and Hell (2021), this occurs due to regions where precipitation is anticorrelated with temperature. Surface dissipation of barotropic energy at large scales induces regions of mechanically forced ascent and subsidence through Ekman pumping. Descending motions in regions of large-scale subsidence induce warm and dry anomalies. Conversely, ascending regions are associated with colder but moister conditions.

Turbulence is characterized by the transport of energy across different scales of motion within the same energy mode. Here, we compute the baroclinic energy flux as

$$\begin{aligned}\mathcal{F}_{\mathrm{bc}} &= -\int_0^K J(\psi'_{\mathrm{BT}}, \mathrm{APE})\Big|_k - J\left(\nabla^2\psi'_{\mathrm{BT}}, \frac{1}{2}|\psi'_{\mathrm{bc}}|^2\right)\Big|_k dK \\ &= \mathcal{F}_{\mathrm{APE}} + \mathcal{F}_{\mathrm{bc},\zeta}.\end{aligned} \tag{39}$$

This flux, which can be further decomposed into an APE component $\mathcal{F}_{\mathrm{APE}}$ and a vorticity component $\mathcal{F}_{\mathrm{bc},\zeta}$, corresponds to the energy transfer across scales. A positive value corresponds to a transfer toward larger wavenumber (and hence smaller scale). As advection conserves the total baroclinic energy, it does not appear in the domain averaged budget Eq. (24). Figure 9 shows these fluxes for increasing values of μ_s. The slope contains information about whether advection is moving energy to (negative slope, dissipation dominates) or from (positive slope, injection dominates) that scale. A well-defined inertial range would exhibit slope zero, indicating that energy is maintained without gain or loss.

As shown in Fig. 9a, the APE cascade $\mathcal{F}_{\mathrm{APE}}$ corresponds to a transfer of energy from large scale, where APE is generated by downgradient heat fluxes, to smaller scales corresponding to the negative slopes at the largest scales. In contrast, the baroclinic vorticity term $\mathcal{F}_{\mathrm{bc},\zeta}$, plotted in Fig. 9b, displays an inverse energy cascade from small to larger scales. The peak of this injection, as with the precipitation, shifts to smaller scales as μ_s increases. The two terms combine in Fig. 9c, which shows a strong convergence of baroclinic energy at scales close to the deformation radius. This convergence spans from roughly the deformation radius scale to half the deformation radius scale in all simulations and is balanced by the baroclinic to barotropic energy conversion term $\mathcal{B}$. Simulations with values of $\mu_s \geq 2$ exhibit another region of energy injection at scales smaller than $K \approx 2\lambda^{-1}$. This corresponds to the scales at which precipitation becomes a dominant source of APE. The absence of a similar region in Fig. 9a indicates that APE generated from precipitation

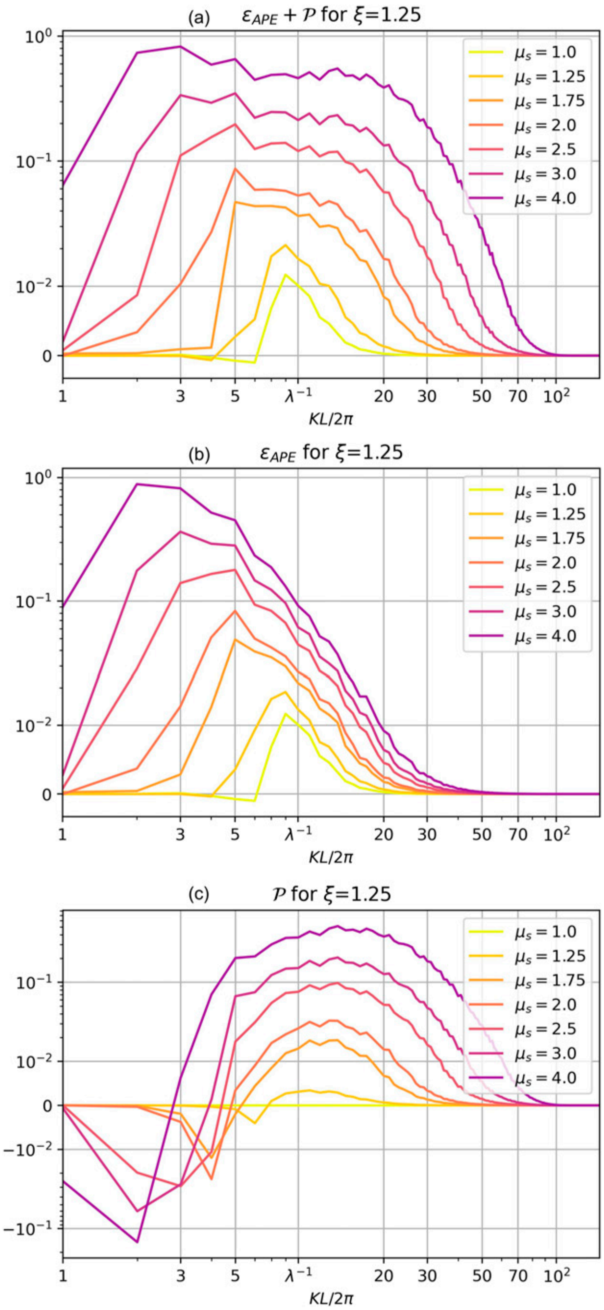

FIG. 8. The spectra of the source terms of the baroclinic energy E_{bc}. These include a downgradient flux of sensible heat $\varepsilon_{\mathrm{APE}}$ and a precipitation injection term $\mathcal{P}$. The y axis is on a symlog scale, such that it is linear for values between ± 0.01.

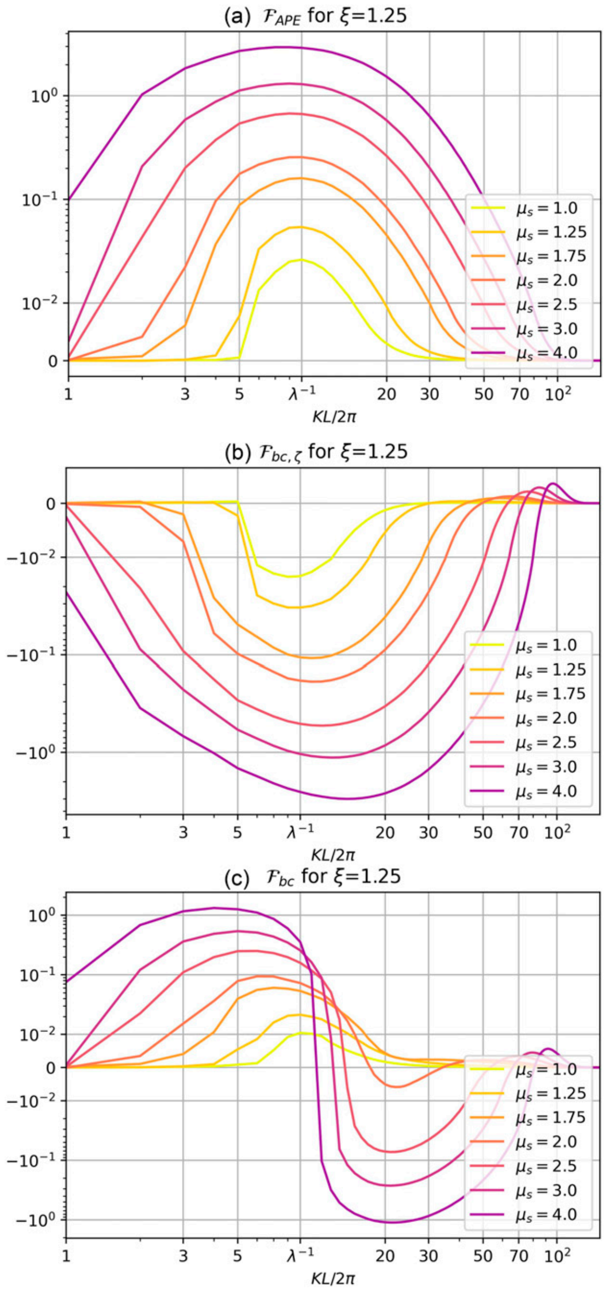

FIG. 9. The advective flux of (a) the APE, (b) the baroclinic kinetic energy, and (c) the total baroclinic energy. The y axis is on a symlog scale, such that it is linear for values between ± 0.1. The advection term transports energy from the scales where the slope is positive to those where the slope is negative. Cascade behavior corresponds to the regions where the slope is near zero, as energy is added and removed at similar rates.

is quickly transferred into the baroclinic vorticity at small scales without further advection.

c. Barotropic energy

The barotropic injection term $\mathcal{B}$ of Eq. (23) can be decomposed into a linear and nonlinear component in spectral space, such that

$$\begin{aligned}\hat{\mathcal{B}}_k &= \hat{\mathcal{B}}_{k,\mathrm{nonlin}} + \hat{\mathcal{B}}_{k,\mathrm{lin}} \\ &= \hat{\psi}^{*\prime}_{\mathrm{BT},k} J(\psi'_{\mathrm{bc}}, \nabla^2 \psi'_{\mathrm{bc}})|_k + \frac{U}{2} K^2 \hat{\psi}^{*\prime}_{\mathrm{BT},k} \hat{\psi}'_{\mathrm{bc},k}.\end{aligned} \tag{40}$$

Here, the subscript k indicates that the term is evaluated at the wavenumber k. Figure 10 demonstrates that both of these

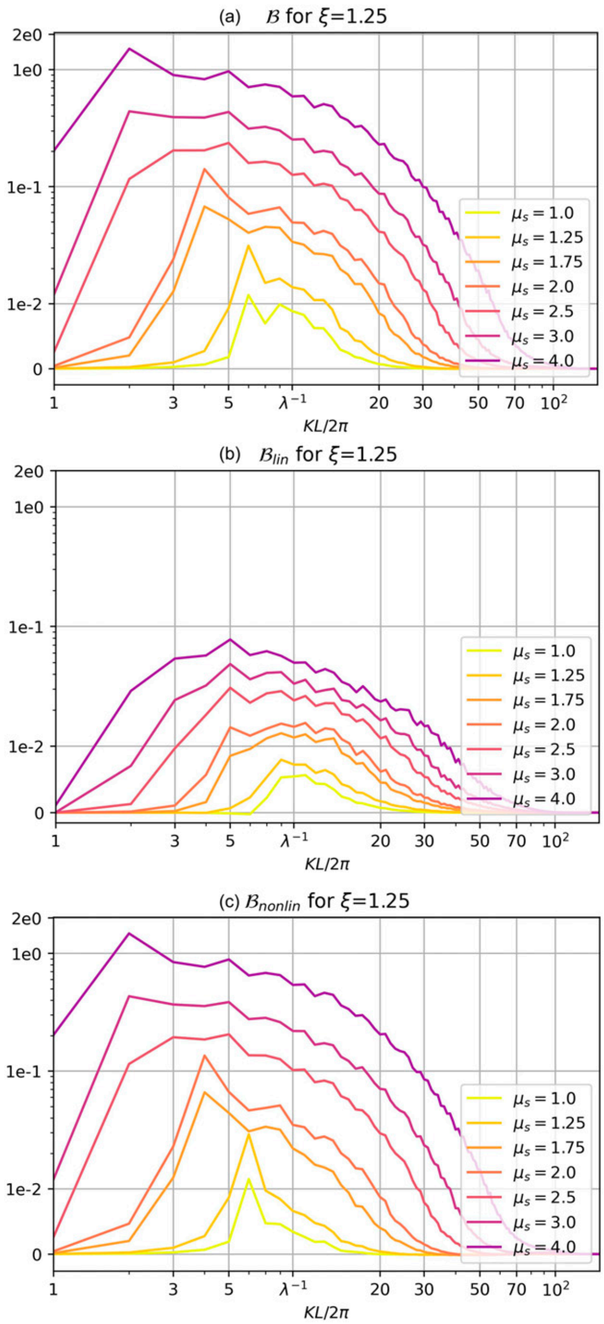

FIG. 10. The injection into the barotropic energy, decomposed into linear and nonlinear components. The y axis is on a symlog scale, such that it is linear for values less than 0.01.

terms exhibit spectral broadening to both larger and smaller scales, while linear stability analysis only predicted a broadening to smaller scales. In fact, increasing the strength of the bulk moisture stratification shifts the peak of energy generation to larger scales. The smaller linear term (Fig. 10b) peaks at smaller scales than the dominant nonlinear term, but still exhibits growth at larger scales. Additionally, the nonlinear term becomes proportionately larger as the value of μ_s increases, from roughly a factor of 2 to 10.

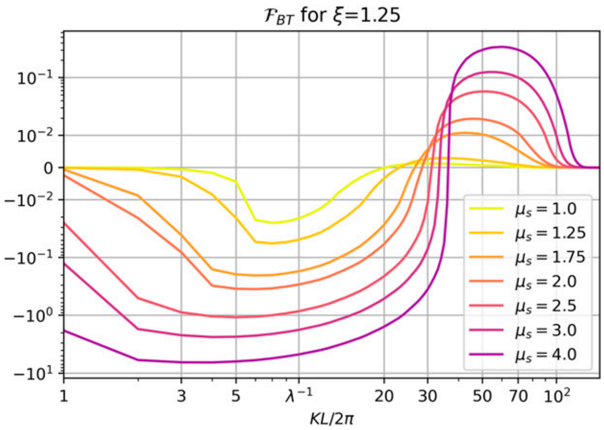

FIG. 11. The advective flux of the barotropic energy. The y axis is on a symlog scale, such that it is linear for values between ± 0.1.

The barotropic energy cascade is characterized by

$$\mathcal{F}_{\rm BT} = -\int_0^K \psi'^{*}_{{\rm BT},k} J(\psi'_{\rm BT}, \nabla^2 \psi'_{\rm BT})|_k dK. \tag{41}$$

This term, shown in Fig. 11, exhibits a forward enstrophy cascade at small scales and an inverse energy cascade at large scales. As μ_s increases, unstable growth occurs at smaller scales, causing the enstrophy cascade to likewise start at smaller scales. At larger scales, a slight positive slope indicates some injection occurring even close to the large-scale cutoff. However, the portion with the steepest positive slope starts at scales near the Rossby radius and extends to smaller scales, even though Fig. 10 shows the largest injection at scales above the Rossby radius. This is consistent with a significant transport of barotropic energy from small scales to the largest relevant scales observed in Fig. 10. This indicates that the system exhibits an inverse cascade—a transport of energy to larger scales—but not a corresponding inertial range. This muddies the scaling arguments for the slope of the inverse cascade, but the arguments for the *termination* of the cascade may still be valid.

d. Rhines scale and the inverse cascade

Held and Larichev (1996) argued that the termination of the inverse cascade in a dry system can be predicted from the criticality. We here test whether a similar argument holds for the saturated system. Their argument equates two approximations of the energy generation rate ε. The first is a dimensional analysis argument which applies when the system has a sufficient inertial range; however, we will relax that assumption here to statistical equilibrium. This approximation is given by

$$\varepsilon \sim V^3 k_0, \tag{42}$$

where V is the RMS barotropic velocity and k_0 is the Rhines scale as defined in Eq. (21). This is an assumption that the energy generation can be approximated by an energy scale $\sim V^2$ and a time scale $\sim (Vk_0)^{-1}$.

The second approximation comes from mixing length theory, which assumes that a tracer anomaly travels a characteristic mixing length before being reassimilated into the large-scale flow. The size of the anomaly can then be approximated by a first-order Taylor expansion, with the gradient of the large-scale background flow dominating the first derivative and the mixing length characterizing the perturbation about the reference position. Held and Larichev (1996) take the Rhines scale to be the mixing length for the baroclinic PV, which at large scales behaves as a passive tracer advected by the dominant barotropic flow. The equivalent argument in the MQG system would predict the same with the MPV, allowing for an estimate of the typical size of its eddies:

$$q'_m \approx -k_0^{-1}\frac{\partial Q_m}{\partial y} \approx k_0^{-1}\mu_s U\lambda^{-2}. \tag{43}$$

The injection into kinetic energy from MAPE can then be approximated as

$$\varepsilon = \varepsilon_{\mathrm{APE}} + \varepsilon_{\mathrm{ME}} = -U\overline{v'_{\mathrm{BT}}q'_m} \approx Vk_0^{-1}\mu_s U^2\lambda^{-2}. \tag{44}$$

Remembering that the criticality is defined as $\xi = U/\beta\lambda^2$ and that Rhines scale is given by Eq. (21), $k_0 = (V/\beta)^{1/2}$, we can combine Eqs. (42) and (44) to yield

$$k_0(\mu_s^{1/2}\lambda) \approx (\mu_s\xi)^{-1}, \tag{45}$$

$$\frac{V}{U} \approx \mu_s\xi, \tag{46}$$

$$\frac{\varepsilon}{U^3\lambda^{-1}} \approx \mu_s^{5/2}\xi^2. \tag{47}$$

These scalings are fully consistent with those of Held and Larichev (1996) after replacing the deformation radius λ by its moist counterpart $\mu_s^{1/2}\lambda$ and the dry supercriticality ξ by the moist supercriticality $\mu_s\xi$.

The first Eq. (45) indicates that the ratio between the Rhines scale and the moist deformation radius $\lambda_s = \mu_s^{1/2}\lambda$ is equal to the moist supercriticality $\mu_s\xi$. It indicates that for a constant temperature gradient, the Rhines scale shifts to larger scale as the humidity gradient increases. The second Eq. (46) indicates that the ratio of RMS barotropic velocity V to the vertical wind shear goes as the moist supercriticality $\mu_s\xi$. Thus, for a constant temperature gradient, the velocity will increase if the humidity gradient increases, e.g., through increasing the global average temperature. Finally, the third Eq. (47) indicates that the energy generation and dissipation ε varies as$\mu_s^{5/2}$, and is thus highly sensitive to the moist parameter μ_s.

These scalings are tested in Fig. 12. As in Held and Larichev (1996), the Rhines scale, RMS barotropic velocity, and energy generation increase faster with criticality than predicted. These arguments should apply best in the asymptotic limit $\xi_s \to \infty$. More data at larger effective criticality would be needed to see if this is the case. A slight shallowing of the slope for values above $\xi_s \approx 4$ indicates that convergence might be possible. At subcriticality, $\xi_s \approx 1$, the barotropic and baroclinic EKE are of

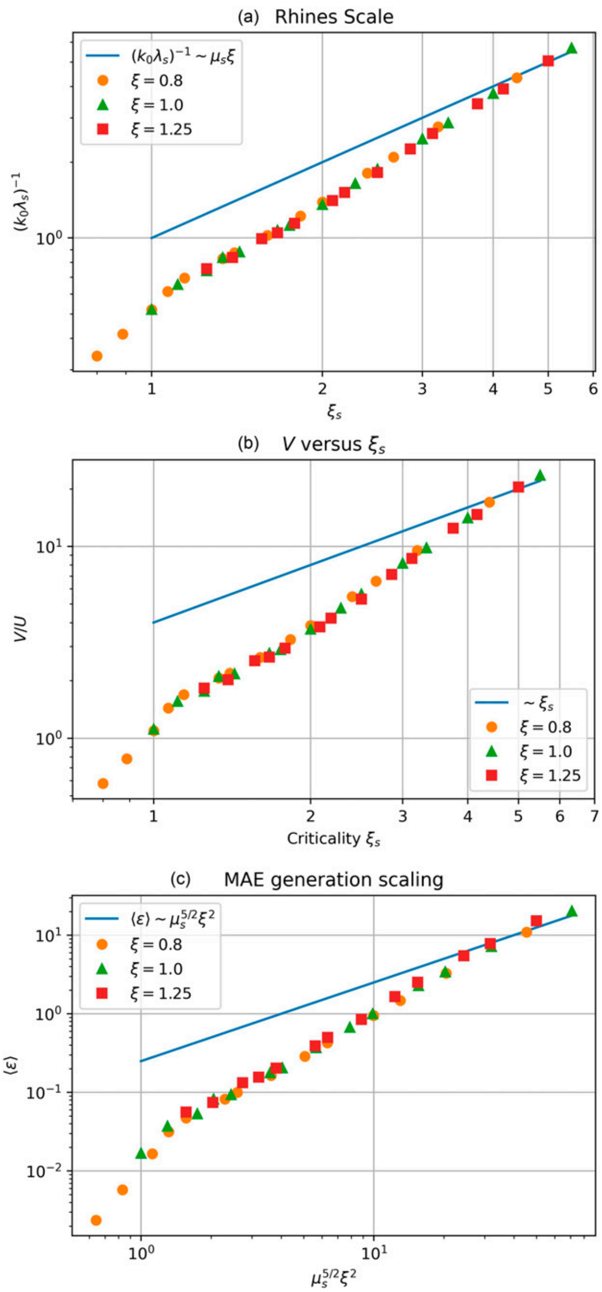

FIG. 12. The scaling of (a) the Rhines scale k_0 computed from the RMS barotropic velocity as a function of saturated criticality, (b) the RMS barotropic velocity V as a function of saturated criticality $\mu_s\xi$, and (c) the total energy generated by the MQG system. Each marker corresponds to a fixed value of dry criticality ξ, indicated in the legend.

similar orders of magnitude. As such, the assumption that the baroclinic PV can be treated as a passive tracer no longer holds.

While the proposed scalings indicate that geostrophic turbulence has a very high sensitivity to moisture content through the parameter μ_s, it should be noted that these scalings only hold in the saturated limit, i.e., in an atmosphere that is raining everywhere. For partial saturation, Lapeyre and Held (2004) show that moist geostrophic turbulence behaves somewhere between the dry and saturated limit. Further investigations of the impacts of moisture on geostrophic turbulence in a partially saturated atmosphere are left to a future study.

6. Conclusions

We have investigated geostrophic turbulence in an idealized moist model analogous to that of Lapeyre and Held (2004). We introduced a framework for the energy centered on the idea that a "condensation level" characterizes a moist energy (ME) that can be transformed into available potential energy (APE) through precipitation. The large-scale gradient of the condensation level provides a reservoir of ME. Eddies extract ME by transporting moisture poleward, which is then converted to APE when precipitation occurs in the warm sector of the eddies. This provides an additional source of baroclinic energy, which can significantly energize moist geostrophic turbulence compared to its dry counterpart under the same temperature gradient. Associated with this new framework is a moist baroclinic potential vorticity which is conserved under latent heat release. This modified PV emphasizes a gradient that takes into account the background meridional configuration of a moist static energy.

By enforcing a high rate of evaporation and a short precipitation relaxation time, we achieve a saturated limit. Under this limit, the MQG system is mathematically equivalent to the dry two-layer QG equations after rescaling both the time and spatial scales. In particular, this saturated limit makes it possible to extend results from geostrophic turbulence to include the effect of moisture on the dynamics of baroclinic eddies.

We analyzed the conditions for baroclinic instability in the saturated limit using a linear stability analysis. We demonstrate that a saturated criticality, the dry criticality rescaled by a parameter μ_s, better predicts instability, including where dry models would predict stability. We confirm numerically that the fully nonlinear MQG system exhibits instability at smaller scales and an increase in the total energy injection. This conclusion is consistent with the results of Emanuel et al. (1987), Fantini (1995), and Joly and Thorpe (1989), among others.

We examined the impacts of moisture on the injection scale and energy cascade by considering the tendency terms in the full nonlinear equations. The inclusion of moisture results in the energy injection into the barotropic mode broadening to both larger and smaller scales than in the dry case. In particular, as the strength of moist parameters increased, precipitation shifts to smaller scales and becomes the dominant contribution to instability. The increase in eddy kinetic energy generation in from latent heat release enhances the inverse cascade of barotropic kinetic energy, similar to the arguments presented in Held and Larichev (1996). In particular, the Rhines scale associated with the end of the inverse cascade shifts to larger scale in the presence of a moisture gradient. We confirmed this numerically by calculating the Rhines scale from the root-mean-square barotropic velocity.

The moist available potential energy (MAPE) defined here is equivalent to the framework of Lapeyre and Held (2004) with different partitioning. In their framework, a moist static energy and a moisture deficit/surplus term form the basis for the quadratics. Ours keeps the dry APE intact and defines ME as a quadratic of the condensation level, which is conserved in the absence of diabatic forcing. Our ME more closely resembles that of tropical models such as Pauluis et al. (2008) and Frierson et al. (2004). Likewise, the ME of Smith and Stechmann (2017) can be reworked into a quadratic of a quantity proportional to the dry potential temperature of a system brought adiabatically to saturation. This partitioning can be of particular use away from the assumption of strict quasi equilibrium and uniform evaporation rate employed here. These assumptions result in a system that acts as a highly efficient moist heat engine. More realistic moist systems are not fully saturated, and as a result, tend to have reduced mechanical efficiency stemming from diabatic processes that primarily act on the ME. This partitioning emphasizes that moisture contributes to the EKE through the precipitation term, and would allow for a direct study of the factors within the ME tendency that reduce the efficiency in a partially saturated system. More work is needed to determine the analog of the ME described here in more realistic models of moist atmospheric dynamics. Based on our results, it is worth exploring whether the lifting condensation level could be used to define a generalized ME.

The moist criticality parameter suggests that the classic baroclinic adjustment arguments, such as in Stone (1978), might be improved upon by a framework which includes the poleward transport of latent heat and its impact of static stability. Baroclinic adjustment predicts that the dry criticality of Earth's atmosphere will remain around $\xi \approx 1$ across different climate forcings. However, if the threshold of instability is instead determined by a moist criticality, this reduces the temperature gradient necessary to trigger efficient heat transport.

For insight, consider a planet warming uniformly at the surface. We can estimate an increase in the moisture availability by 7% K^{-1}, translating to a comparable increase in the gradient. Naively, one could start by simply increasing parameter μ_s, leaving the temperature gradient fixed (i.e., fixed dry criticality ξ). This will lead to greater instability and more energy transport poleward. The increase in meridional heat transport, however, would demand a change in the energy balance at the top of the atmosphere. If we instead assume that the top of the atmosphere balance remains about the same, then it is the total meridional transport of energy that is fixed. If the energy transport scales with the saturated criticality $\xi_s = \mu_s \xi$, then the dry criticality decreases proportionately to compensate for the increase in the moisture gradient.

Further research could help clarify the results of this study and its connections to other work. Our spectral analysis partially supports the findings of studies like Bembenek et al. (2020) and Lutsko and Hell (2021), but a more direct comparison can be achieved by applying our energetic framework to partially saturated systems with nonhomogeneous background states. Additionally, warming predicts an increase in both the dry static stability and the moisture content (Frierson et al. 2006). As such, the *absolute* scale changes may differ from the relative changes described here. Indeed, studies that consider the case where moisture compensates for changes in dry static stability (Zurita-Gotor 2005; Juckes 2000; Moore and Montgomery 2004) often reach opposite conclusions to ours.

Another natural follow-up is the case of partial saturation, which introduces additional complications. The decorrelation of moisture from temperature adds an additional degree of freedom, requiring a full consideration of the corresponding terms in the energy and moist PV that were neglected here. This opens new possibilities for the cascade behavior of ME, which could result in energy generation at scales smaller than those predicted in either the dry or saturated case. The energetic framework provided here can be used to analyze these additional terms and determine the changes to scalings associated with them.

Acknowledgments. We thank Shafer Smith for guidance on turbulence and implementing QG, and Ángel F. Adames-Corraliza and two anonymous reviewers for helpful comments on a previous version of this manuscript. MLB and EPG acknowledge support from the U.S. National Science Foundation through Award AGS-1852727. MLB and OP acknowledge support from the National Science Foundation under Grant HDR-1940145 and from the New York University in Abu Dhabi Research Institute under Grant G1102.

Data availability statement. The code used to generate the data in this study is stored in the repository at https://github.com/margueriti/Moist_QG_public.

APPENDIX A

Equivalence of Dry and Saturated Limits

We introduce some rescalings to nondimensionalize:

$$(x, y) \to \lambda^{-1}(x, y), \tag{A1}$$

$$t \to U\lambda^{-1}t, \tag{A2}$$

$$\beta \to U^{-1}\lambda^2\beta = \xi^{-1}, \tag{A3}$$

$$r \to U^{-1}\lambda r, \tag{A4}$$

$$\psi \to U^{-1}\lambda^{-1}\psi, \tag{A5}$$

$$q \to U^{-1}\lambda q, \tag{A6}$$

$$\eta \to U^{-1}\lambda f_0 \eta, \tag{A7}$$

$$W \to U^{-2}\lambda^2 f_0 \frac{W}{H}, \tag{A8}$$

$$m \to U^{-1}\lambda f_0 m/H, \tag{A9}$$

$$P \to U^{-2}\lambda^2 f_0 P/H, \tag{A10}$$

with λ and U, respectively, the reference length and velocity scales, rescaled as the unit. The resulting perturbation equations can then be written as

$$\frac{D_{\rm BT}q'_{\rm BT}}{Dt} = -J(\psi'_{\rm bc}, q'_{\rm bc}) - \frac{1}{2}\partial_x\nabla^2\psi'_{\rm bc} - \xi^{-1}\partial_x\psi'_{\rm BT} - \frac{r}{2}\nabla^2\psi'_2, \tag{A11}$$

$$\frac{D_{\rm BT}q'_{\rm bc}}{Dt} = -J(\psi'_{\rm bc}, q'_{\rm BT}) - \frac{1}{2}\partial_x q'_{\rm BT} - \xi^{-1}\partial_x\psi'_{\rm bc} - \partial_x\psi'_{\rm BT} + \frac{r}{2}\nabla^2\psi'_2 - \mathcal{L}P', \tag{A12}$$

$$\frac{D_{\rm BT}\eta'}{Dt} = v'_{\rm BT} - W + \mathcal{L}P', \tag{A13}$$

$$\frac{D_{\rm BT}m'}{Dt} = +J(\psi'_{\rm bc}, m') + \frac{1}{2}\partial_x m' + \mathcal{C}(v'_{\rm BT} - v'_{\rm bc}) - P' + W, \tag{A14}$$

$$\frac{D_{\rm BT}q'_m}{Dt} = -J\left(\psi'_{\rm bc}, q'_{\rm BT} - \frac{\mathcal{L}}{1-\mathcal{L}}m'\right) - \frac{1}{2}\partial_x q'_{\rm BT} - \xi^{-1}\partial_x\psi'_{\rm bc} - \mu_s v'_{\rm BT} + \frac{1}{2}\frac{\mathcal{L}}{1-\mathcal{L}}\partial_x(m' - m'_s) + \frac{r}{2}\nabla^2\psi'_2, \tag{A15}$$

where the operator $D_{\rm BT}/Dt$ denotes advection by the barotropic flow. In an atmosphere that is everywhere at saturation, the moist baroclinic potential vorticity becomes

$$q'_m = \nabla^2\psi'_{\rm bc} - 2\mu_s\lambda^{-2}\psi'_{\rm bc}, \tag{A16}$$

with governing equation

$$\frac{D_{\rm BT}q'_m}{Dt} = -J(\psi'_{\rm bc}, q'_{\rm BT}) - \frac{1}{2}\partial_x q'_{\rm BT} - \xi^{-1}\partial_x\psi'_{\rm bc} - \frac{1+\mathcal{CL}}{1-\mathcal{L}}\partial_x\psi'_{\rm BT} + \frac{r}{2}\nabla^2\psi'_2, \tag{A17}$$

which closely resembles the baroclinic mode except for one term with a factor of $\mu_s = (1+\mathcal{CL})/(1-\mathcal{L})$. If we instead scale the length by $\lambda_s = \mu_s^{-1/2}\lambda$ and substitute accordingly in all other rescalings, the governing equation for moist baroclinic PV at saturation then becomes

$$\partial_t q'_m + J(\psi'_{\rm BT}, q'_m) = -J(\psi'_{\rm bc}, q'_{\rm BT}) - \frac{1}{2}\partial_x q'_{\rm BT} - \xi_s^{-1}\partial_x\psi'_{\rm bc} - \partial_x\psi'_{\rm BT} + \frac{r}{2}\nabla^2\psi'_2. \tag{A18}$$

Noting that $J(\psi'_{\rm bc}, q'_{\rm bc}) = J(\psi'_{\rm bc}, \nabla^2\psi'_{\rm bc}) = J(\psi'_{\rm bc}, q'_m)|_{\rm sat}$, the barotropic mode is unchanged under the rescaling and can be thought of as forced by the moist baroclinic mode. Hence, we have a closed pair of governing equations identical to the governing equations for the dry two-layer baroclinic instability, and so the saturated limit is equivalent to the dry case with a rescaling.

In particular, the linearized forms of Eqs. (A11) and (A18) can be written as

$$\partial_t q'_{\mathrm{BT}} = -\frac{1}{2}\partial_x \nabla^2 \psi'_{\mathrm{bc}} - \xi_s^{-1}\partial_x \psi'_{\mathrm{BT}}, \tag{A19}$$

$$\partial_t q'_m = -\frac{1}{2}\partial_x q'_{\mathrm{BT}} - \xi_s^{-1}\partial_x \psi'_{\mathrm{bc}} - \partial_x \psi'_{\mathrm{BT}}. \tag{A20}$$

Here, we neglect the Ekman dissipation term for simplicity. In spectral space, this becomes

$$-i\omega\begin{pmatrix} -K^2 & 0 \\ 0 & -K^2 - 1 \end{pmatrix}\begin{pmatrix} \hat{\psi}'_{\mathrm{BT},k} \\ \hat{\psi}'_{\mathrm{bc},k} \end{pmatrix} = \begin{bmatrix} -ik\xi_s^{-1} & ikK^2/2 \\ ik(K^2/2 - 1) & -ik\xi_s^{-1} \end{bmatrix}\begin{pmatrix} \hat{\psi}'_{\mathrm{BT},k} \\ \hat{\psi}'_{\mathrm{bc},k} \end{pmatrix}. \tag{A21}$$

Recalling that the growth rate $\sigma = -\mathrm{Re}(i\omega)$ and redimensionalizing where relevant, the above can then be used to solve for Eq. (35).

APPENDIX B

Omega Equation

We do not directly use the vertical velocity W in any of our diagnostics here. Nonetheless, it can be diagnosed by the omega equation, given by

$$f_0\left(1 - \frac{\lambda^2}{2}\nabla^2\right)W = -J(\psi_{\mathrm{BT}}, \zeta_{\mathrm{bc}}) - J(\psi_{\mathrm{bc}}, \zeta_{\mathrm{BT}} + \beta y) + \nabla^2 J(\psi_{\mathrm{BT}}, \psi_{\mathrm{bc}}) - \frac{\lambda^2 f_0}{2H}\mathcal{L}\nabla^2(P - E). \tag{B1}$$

APPENDIX C

Precipitation Closure

We use the closure described in Lapeyre and Held (2004), based on the idea of conservation of effective thickness in the domain average:

$$\partial_t\overline{(\eta + \mathcal{L}m)} = 0. \tag{C1}$$

Hence if we pick an initial value $\overline{\eta + \mathcal{L}m} = 0$, we can expect this quantity to be conserved over time. These domain averages then evolve with the precipitation and evaporation as

$$\partial_t\overline{m} = \overline{E - P}$$
$$\partial_t\overline{\eta} = \mathcal{L}(\overline{P - E}). \tag{C2}$$

Hence the total precipitation can be expressed as

$$P = \begin{cases} [(1 + \mathcal{CL})\overline{m} + m' - \mathcal{C}\eta']/\tau & \text{where } m > m_s \\ 0 & \text{where } m \le m_s \end{cases}. \tag{C3}$$

REFERENCES

Adames, Á. F., 2021: Interactions between water vapor, potential vorticity, and vertical wind shear in quasi-geostrophic motions: Implications for rotational tropical motion systems. *J. Atmos. Sci.*, **78**, 903–923, https://doi.org/10.1175/JAS-D-20-0205.1.

——, and Y. Ming, 2018: Interactions between water vapor and potential vorticity in synoptic-scale monsoonal disturbances: Moisture vortex instability. *J. Atmos. Sci.*, **75**, 2083–2106, https://doi.org/10.1175/JAS-D-17-0310.1.

Bembenek, E., D. N. Straub, and T. M. Merlis, 2020: Effects of moisture in a two-layer model of the midlatitude jet stream. *J. Atmos. Sci.*, **77**, 131–147, https://doi.org/10.1175/JAS-D-19-0021.1.

Betts, A. K., and M. J. Miller, 1986: A new convective adjustment scheme. Part II: Single column tests using GATE wave, BOMEX, ACTEX and arctic air-mass data sets. *Quart. J. Roy. Meteor. Soc.*, **112**, 693–709, https://doi.org/10.1002/qj.49711247308.

Bretherton, C. S., M. E. Peters, and L. E. Back, 2004: Relationships between water vapor path and precipitation over the tropical oceans. *J. Climate*, **17**, 1517–1528, https://doi.org/10.1175/1520-0442(2004)017<1517:RBWVPA>2.0.CO;2.

de Vries, H., J. Methven, T. H. A. Frame, and B. J. Hoskins, 2010: Baroclinic waves with parameterized effects of moisture interpreted using Rossby wave components. *J. Atmos. Sci.*, **67**, 2766–2784, https://doi.org/10.1175/2010JAS3410.1.

Edwards, T. K., L. M. Smith, and S. N. Stechmann, 2019: Spectra of atmospheric water in precipitating quasi-geostrophic turbulence. *Geophys. Astrophys. Fluid Dyn.*, **114**, 715–741, https://doi.org/10.1080/03091929.2019.1692205.

Emanuel, K. A., M. Fantini, and A. J. Thorpe, 1987: Baroclinic instability in an environment of small stability to slantwise moist convection. Part I: Two-dimensional models. *J. Atmos. Sci.*, **44**, 1559–1573, https://doi.org/10.1175/1520-0469(1987)044<1559:BIIAEO>2.0.CO;2.

——, J. D. Neelin, and C. S. Bretherton, 1994: On large-scale circulations in convecting atmospheres. *Quart. J. Roy. Meteor. Soc.*, **120**, 1111–1143, https://doi.org/10.1002/qj.49712051902.

Fantini, M., 1990: Nongeostrophic corrections to the eigensolutions of a moist baroclinic instability problem. *J. Atmos. Sci.*, **47**, 1277–1287, https://doi.org/10.1175/1520-0469(1990)047<1277:NCTTEO>2.0.CO;2.

——, 1995: Moist Eady waves in a quasigeostrophic three-dimensional model. *J. Atmos. Sci.*, **52**, 2473–2485, https://doi.org/10.1175/1520-0469(1995)052<2473:MEWIAQ>2.0.CO;2.

Frierson, D. M. W., A. J. Majda, and O. M. Pauluis, 2004: Large scale dynamics of precipitation fronts in the tropical atmosphere: A novel relaxation limit. *Commun. Math. Sci.*, **2**, 591–626, https://doi.org/10.4310/CMS.2004.v2.n4.a3.

——, I. M. Held, and P. Zurita-Gotor, 2006: A gray-radiation aquaplanet moist GCM. Part I: Static stability and eddy scale. *J. Atmos. Sci.*, **63**, 2548–2566, https://doi.org/10.1175/JAS3753.1.

Held, I. M., and V. D. Larichev, 1996: A scaling theory for horizontally homogeneous, baroclinically unstable flow on a beta plane. *J. Atmos. Sci.*, **53**, 946–952, https://doi.org/10.1175/1520-0469(1996)053<0946:ASTFHH>2.0.CO;2.

Inoue, K., and L. E. Back, 2015: Gross moist stability assessment during TOGA COARE: Various interpretations of gross moist stability. *J. Atmos. Sci.*, **72**, 4148–4166, https://doi.org/10.1175/JAS-D-15-0092.1.

——, and ——, 2017: Gross moist stability analysis: Assessment of satellite-based products in the GMS plane. *J. Atmos. Sci.*, **74**, 1819–1837, https://doi.org/10.1175/JAS-D-16-0218.1.

Joly, A., and A. J. Thorpe, 1989: Warm and occluded fronts in two-dimensional moist baroclinic instability. *Quart. J. Roy. Meteor. Soc.*, **115**, 513–534, https://doi.org/10.1002/qj.49711548705.

Juckes, M. N., 2000: The static stability of the midlatitude troposphere: The relevance of moisture. *J. Atmos. Sci.*, **57**, 3050–3057, https://doi.org/10.1175/1520-0469(2000)057<3050:TSSOTM>2.0.CO;2.

Lambaerts, J., G. Lapeyre, and V. Zeitlin, 2011: Moist versus dry barotropic instability in a shallow-water model of the atmosphere with moist convection. *J. Atmos. Sci.*, **68**, 1234–1252, https://doi.org/10.1175/2011JAS3540.1.

——, ——, and ——, 2012: Moist versus dry baroclinic instability in a simplified two-layer atmospheric model with condensation and latent heat release. *J. Atmos. Sci.*, **69**, 1405–1426, https://doi.org/10.1175/JAS-D-11-0205.1.

Lapeyre, G., and I. M. Held, 2004: The role of moisture in the dynamics and energetics of turbulent baroclinic eddies. *J. Atmos. Sci.*, **61**, 1693–1710, https://doi.org/10.1175/1520-0469(2004)061<1693:TROMIT>2.0.CO;2.

Lutsko, N. J., and M. C. Hell, 2021: Moisture and the persistence of annular modes. *J. Atmos. Sci.*, **78**, 3951–3964, https://doi.org/10.1175/JAS-D-21-0055.1.

Moore, R. W., and M. T. Montgomery, 2004: Reexamining the dynamics of short-scale, diabatic Rossby waves and their role in midlatitude moist cyclogenesis. *J. Atmos. Sci.*, **61**, 754–768, https://doi.org/10.1175/1520-0469(2004)061<0754:RTDOSD>2.0.CO;2.

Neelin, J. D., and I. M. Held, 1987: Modeling tropical convergence based on the moist static energy budget. *Mon. Wea. Rev.*, **115**, 3–12, https://doi.org/10.1175/1520-0493(1987)115<0003:MTCBOT>2.0.CO;2.

Parker, D. J., and A. J. Thorpe, 1995: Conditional convective heating in a baroclinic atmosphere: A model of convective frontogenesis. *J. Atmos. Sci.*, **52**, 1699–1711, https://doi.org/10.1175/1520-0469(1995)052<1699:CCHIAB>2.0.CO;2.

Pauluis, O., D. M. W. Frierson, and A. J. Majda, 2008: Precipitation fronts and the reflection and transmission of tropical disturbances. *Quart. J. Roy. Meteor. Soc.*, **134**, 913–930, https://doi.org/10.1002/qj.250.

——, A. Czaja, and R. Korty, 2010: The global atmospheric circulation in moist isentropic coordinates. *J. Climate*, **23**, 3077–3093, https://doi.org/10.1175/2009JCLI2789.1.

Schneider, T., and P. A. O'Gorman, 2008: Moist convection and the thermal stratification of the extratropical troposphere. *J. Atmos. Sci.*, **65**, 3571–3583, https://doi.org/10.1175/2008JAS2652.1.

Shaw, T. A., and Coauthors, 2016: Storm track processes and the opposing influences of climate change. *Nat. Geosci.*, **9**, 656–664, https://doi.org/10.1038/ngeo2783.

Smith, L. M., and S. N. Stechmann, 2017: Precipitating quasigeostrophic equations and potential vorticity inversion with phase changes. *J. Atmos. Sci.*, **74**, 3285–3303, https://doi.org/10.1175/JAS-D-17-0023.1.

Stone, P. H., 1978: Baroclinic adjustment. *J. Atmos. Sci.*, **35**, 561–571, https://doi.org/10.1175/1520-0469(1978)035<0561:BA>2.0.CO;2.

Vallis, G. K., 2006: *Atmospheric and Oceanic Fluid Dynamics: Fundamentals and Large-Scale Circulation*. 1st ed. Cambridge University Press, 769 pp.

Wu, Y., and O. Pauluis, 2014: Midlatitude tropopause and low-level moisture. *J. Atmos. Sci.*, **71**, 1187–1200, https://doi.org/10.1175/JAS-D-13-0154.1.

Zurita-Gotor, P., 2005: Updraft/downdraft constraints for moist baroclinic modes and their implications for the short-wave cutoff and maximum growth rate. *J. Atmos. Sci.*, **62**, 4450–4458, https://doi.org/10.1175/JAS3630.1.